RSC Advances

PAPER

View Article Online
View Journal | View Issue

Cite this: *RSC Adv.*, 2022, **12**, 14183

Direct synthesis of ultrathin FER zeolite nanosheets *via* a dual-template approach†

Yuekun Li,[ab] Duozheng Ma,[ab] Wenhua Fu,[b] Chuang Liu,[b] Yu Wang,[b] Zhendong Wang *[b] and Weimin Yang*[ab]

The synthesis of zeolites with nanosheet morphology has been attracting extensive attention. Despite the steady progress, the direct synthesis of ultrathin nanosheets of **FER** zeolite with thickness of less than 10 nm is still a great challenge. Herein we report a facile synthesis of **FER** zeolite nanosheets (named SCM-37) by using octyltrimethylammonium chloride (OTMAC) and 4-dimethylaminopyridine (4-DMAP) as dual organic templates. The effects of synthesis parameters, including initial molar ratio of SiO_2/Al_2O_3, crystallization temperature and time were investigated. It turned out that the crystallization field of SCM-37 was narrow. A two-step crystallization method was utilized to obtain pure and completely crystallized SCM-37 zeolite. SCM-37 was characterized by multiple techniques, including X-ray powder diffraction (XRD), scanning electron microscopy (SEM), transmission electron microscopy (TEM), nitrogen physisorption, Fourier transform infrared (FTIR), ammonia-temperature programmed desorption (NH_3-TPD) and nuclear magnetic resonance (NMR), and compared with the conventional **FER** zeolite (C-**FER**). The two most significant features of SCM-37 are the ultrathin crystal nanosheet and extremely high external surface area. The thickness of SCM-37 along the *a*-axis is 4∼7 nm, while that of C-**FER** is over 20 nm. The external surface area reaches 198 $m^2\ g^{-1}$, which is over ten times larger than that of C-**FER**. The catalytic performances of the **FER** zeolites were evaluated by the cracking of 1,3,5-triisopropylbenzene (T*i*PB). Although possessing a lower amount of total acid sites, SCM-37 showed higher conversion of T*i*PB, as well as selectivity to the deep cracking products. The superior performance of SCM-37 was attributed to the higher external surface area arising from the ultrathin nanosheets.

Received 28th February 2022
Accepted 29th April 2022

DOI: 10.1039/d2ra01334g

rsc.li/rsc-advances

Introduction

Zeolites are a class of crystalline microporous materials composed of SiO_4 and AlO_4 tetrahedras,[1–4] which are widely used in many fields such as catalysis, ion exchange, and adsorption/separation owing to their tunable chemical composition, strong acidity, excellent thermal/hydrothermal stability and uniform apertures.[5–10] The nanopores of zeolites, diameters of which are usually below 1 nm, offer excellent places for shape-selective catalysis.[11,12] However, zeolites also suffer from intracrystalline diffusion limitations because of the poor accessibility of confined active sites. To shorten the diffusion path and boost the diffusion efficiency consequently, significant efforts have been made to prepare nanosized zeolites, such as nanoparticles, nanoneedles, nanosheets, single-walled zeolitic nanotubes, and zeolites with hollow structure.[13–19]

FER zeolite is composed of 10-membered ring (10-MR) channels (0.43 × 0.55 nm) in the [001] direction and 8-MR channels (0.35 × 0.48 nm) in the [010] direction to form a two-dimensional (2D) channel system (Scheme 1).[20,21] The 6-MR channel parallel to the 10-MR channel intersects with the 8-MR channel to form an ellipsoidal cage of 0.6 to 0.7 nm (fer cage).[22,23] It is effective in diverse catalytic processes, such as skeletal isomerization,[24–26] benzylation,[27] NOx reduction[28] and carbonylation of dimethyl ether.[29–32] To overcome diffusion limitation, **FER** zeolites with nanosized crystals are highly desirable. Although **FER** zeolites can be hydrothermally synthesized using various organic structure-directing agents (OSDAs),[33–36] also called templates, researches on the direct synthesis of ultrathin nanosheets of **FER** zeolite are still rather limited. The general strategy for preparing ultrathin **FER** zeolites nanosheets is to employ elaborately designed OSDAs or introduce surfactants as additive. Using piperidine (PI) and tetramethylammonium hydroxide (TMAOH) as cooperative OSDAs, **FER** nanosheets with hierarchical pores were synthesized. The size of crystals was about 10∼15 μm, while the thickness was less than 50 nm.[22] Hong and coworkers used

[a]*School of Chemical Engineering, East China University of Science and Technology, Shanghai, 200237, PR China. E-mail: yangwm.sshy@sinopec.com*
[b]*State Key Laboratory of Green Chemical Engineering and Industrial Catalysis, Sinopec Shanghai Research Institute of Petrochemical Technology, Shanghai, 201208, PR China. E-mail: wangzd.sshy@sinopec.com*

† Electronic supplementary information (ESI) available. See https://doi.org/10.1039/d2ra01334g

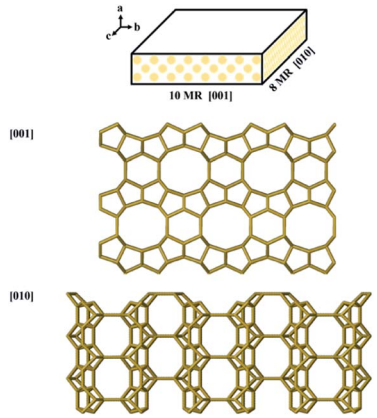

Scheme 1 Structure of FER in the [001] and [010] directions.

choline as a single organic template to synthesize nano-needle like **FER** zeolite (**FER** nanoneedles) with a diameter of 10 nm.[37] Corma and coworkers prepared **FER** nanocrystals with bc flane as low as 10 × 10 nm with the presences of both PI and cetylmethylpiperidinium bromide (C_{16}MPip) as OSDAs.[38] **FER** nanosheets with a thickness of about 10 nm were synthesized by using PI as OSDA and cetyltrimethyl ammonium bromide (CTAB) as morphology regulator.[39] Xiao and coworkers reported a method to synthesize the ultrathin **FER** nanosheets using *N*,*N*-diethyl-*cis*-2,6-dimethyl piperidinium (DMP) as OSDA, which not only directed the crystallization of **FER** zeolite structure, but also inhibited the growth of **FER** zeolite in [100] direction.[40] Wu and coworkers synthesized highly delaminated **FER** nanosheets using a simple imidazole molecule as the single OSDA.[41]

Here we report a new dual-template method for the direct synthesis of ultrathin **FER** zeolite nanosheets, designated as SCM-37 (Sinopec Composite Material No. 37), by using both octyltrimethylammonium chloride (OTMAC) and 4-dimethylaminopyridine (4-DMAP) as templates. Compared to conventional **FER** zeolites (C-**FER**), SCM-37 showed significantly better performance in the catalytic cracking of 1,3,5-triisopropylbenzene (1,3,5-T*i*PB).

Experimental

Synthesis of zeolite

In a typical synthesis of SCM-37, colloidal silica solution (40.0 wt% SiO_2, LUDOX HS40, Aldrich), sodium aluminate (≥41% Al_2O_3, China Medicine (Group) Shanghai Chemical Reagent Co., Ltd), NaOH (99.5% NaOH, China Medicine (Group) Shanghai Chemical Reagent Co., Ltd), octyltrimethylammonium chloride (OTMAC, 99 wt%, Aladdin), 4-dimethylaminopyridine (4-DMAP, 99 wt%, TCI shanghai) and deionized water were mixed in a certain order to obtain the synthesis mixture with molar composition of 1.0 SiO_2: 0.04 Al_2O_3: 0.18 NaOH: 0.30 OTMAC: 0.20 4-DMAP: 20 H_2O. After stirring at room temperature for 3 h, the final synthesis mixture was transferred into a Teflon-lined stainless steel autoclave and crystallized dynamically (20 rpm) at 150 °C for 6 days followed by at 170 °C for 3 days. The obtained solid product was recovered by centrifugation, washed repeatedly with deionized water, and dried overnight at 90 °C. The product was calcined at 550 °C for 6 h to remove the organic species. The obtained sample was denoted as SCM-37.

The conventional **FER** zeolite (denoted as C-**FER**) was prepared according to the previous literature, where cyclohexylamine (CHA) was used as OSDA.[36] The molar composition of the initial gel was 1.0 SiO_2: 0.04 Al_2O_3: 0.20 NaOH: 0.20 CHA: 20 H_2O.

The H-form zeolite samples were obtained by ion-exchanging the calcined samples in 0.5 M NH_4Cl solution at 70 °C for 2 h with solid-to-liquid weight ratio of 1 : 20. The ion-exchange procedure was repeated twice. After that, the solid was recovered by centrifugation, washed, and then dried overnight at 90 °C and calcined at 550 °C for 6 h.

Physicochemical characterization

X-ray powder diffraction (XRD) patterns were recorded on a PANalytical X'Pert PRO diffractometer (Holland) with Cu Kα radiation ($\lambda = 1.54$ Å), operating at 40 kV and 40 mA. The data were collected in 2θ range of 3–50° at a speed of 10° min^{-1}.

The morphology and size of zeolite sample were observed by scanning electron microscopy (SEM) on a Hitachi S-4800 microscope under accelerated voltage of 3.0 kV.

The high-resolution transmission electron microscopy (HRTEM) images were collected under a Cs-corrected STEM (FEI Titan Cubed Themis G2 300) operated at 300 kV with a convergence semi-angle of 25 mrad.

Nitrogen adsorption/desorption analysis was carried out at −196 °C on a BELSORP-MAX instrument after the sample was degassed under vacuum at 300 °C for 5 h. The specific surface area was calculated with the BET equation while the microporous volume was distinguished from the mesoporous one by the *t*-plot method.

Acidity was measured by temperature-programmed desorption of ammonia (NH_3-TPD) with an Altamira AMI-3300 chemisorption equipment equipped with a thermal conductivity detector (TCD). Typically, 100 mg of sample was pre-treated in the helium stream (30 mL min^{-1}) at 550 °C for 1 h. The adsorption of NH_3 (30 mL min^{-1}) was carried out at 100 °C for 30 min. The sample was flushed with helium at 100 °C for 1 h to remove the physisorbed NH_3 from the catalyst. The TPD profile was recorded at a heating rate of 10 °C min^{-1} from 100 °C to 600 °C.

SiO_2/Al_2O_3 molar ratio (SAR) of the prepared **FER** zeolites was quantified by inductive coupled plasma atomic emission spectrometer (ICP-AES) on a Varian 725-ES after dissolving the samples in HF solution.

IR spectra of hydroxyl (4000–2800 cm^{-1}) stretching were all recorded on a Nicolet 5700 FTIR spectrometer.

The nature and concentration of acid sites of the samples were characterized by Fourier transformed infrared spectra after adsorption of pyridine molecule (Py-IR), using a Nicolet Nexus spectrometer equipped with an *in situ* vacuum system containing a secondary vacuum. Wafers with a weight of 15 mg and a diameter of 13 mm were pre-treated under vacuum at

400 °C for 2 h (background spectrum). Then the samples were cooled to 150 °C to adsorb pyridine probe molecules. After that, the samples were thermally desorbed at different temperatures (150 °C and 350 °C) followed by the spectra recording. The concentrations of Brønsted acid sites (B acid) and Lewis acid sites (L acid) were calculated by comparing the integrated areas of the bands at 1545 cm^{-1} and 1455 cm^{-1}. For calculation, integration distinct molar extinction coefficients of 1.67 and 2.22 cm for pyridine interacting with B acid and L acid centers were used, respectively.

^{27}Al and ^{13}C solid-state magic angle spinning solid nuclear magnetic resonance (MAS NMR) spectra were recorded on a JNM-ECZ500R/S1 (JEOL) spectrometer under one-pulse condition. The ^{13}C MAS NMR spectra were recorded at a ^{13}C frequency of 125.765 MHz and a spinning rate of 18.0 kHz with a $\pi/2$ rad pulse length of 5.0 μs, ^{13}C chemical shifts were reported relative to adamantane (ADA). The ^{27}Al MAS NMR spectra were recorded at a ^{27}Al frequency of 130.322 MHz and a spinning rate of 18.0 kHz with a $\pi/2$ rad pulse length of 1.4 μs, the ^{27}Al chemical shifts were referenced to an $Al(NO_3)_3$ solution (1 M).

Catalytic test

Cracking of 1,3,5-triisopropylbenzene (T*i*PB) was used as the probe reaction to evaluate the catalytic property of zeolite. The reaction was carried out in a fixed-bed pulse microreactor with an inner diameter of 6 mm equipped with an Agilent automatic liquid sampler (ALS). Before catalytic test, zeolite powder was pressurized into wafers and crushed and sieved to 40–60 meshes. In a typical test, 50 mg catalyst was mixed with 100 mg of quartz sand and loaded in the reactor, 1 μL of T*i*PB was injected *via* ALS at certain temperature (250 °C, 275 °C, 300 °C, 325 °C, and 350 °C). The result of the first pules at each temperature was analyzed using Agilent 8840 gas chromatograph (GC) apparatus equipped with a flame ionization detector (FID).

The conversion of T*i*PB and selectivity to isopropylbenzene and benzene (*i*PB + Bz) were calculated as follows:

$$\text{Conversion}\% = \left(1 - \frac{c_{TiPB}}{\sum c_i}\right) \times 100\% \quad (1)$$

$$\text{Selectivity}\% = \frac{c_{iPB} + c_{Bz}}{\sum c_i - c_{TiPB}} \times 100\% \quad (2)$$

C_i represents the molar concentration of product i with benzenic ring in the effluents.

Results and discussion

The effect of initial molar ratio of silica to alumina (SAR) on the products was studied. Fig. 1 illustrates the XRD patterns of as-synthesized zeolites with different SAR, as well as that of C-**FER** sample and the simulated pattern of **FER** zeolite. All the samples show patterns corresponding to **FER** type structure with characteristic diffraction peaks at 2θ of 9.4°, 22.3° and 25.2° ascribed to (200), (031) and (040) plane, respectively. No visible diffraction peaks assigned to other zeolites were

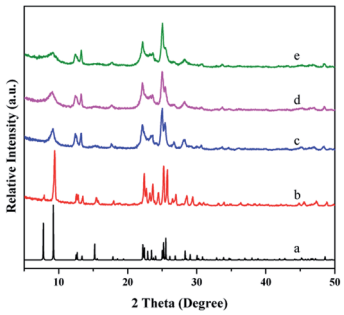

Fig. 1 XRD patterns of simulated **FER** (a), as-synthesized C-**FER** (b) and SCM-37 zeolites with different SAR of 15 (c), 20 (d), 25 (e).

detected, which suggests the purity of all **FER** zeolite materials. The full width at half maximum (FWHM) of the peak at around 9.4° associated with (200) becomes obviously higher with the increase of SAR, which suggests a remarkable loss of ordering along the [100] direction and a decrease of crystal thickness.[21] The broadening of the (200) plane associated peak was also observed in the preparation of other **FER** zeolites with nanosheet morphology.[40] After calcination, SCM-37 samples kept the **FER** framework without any skeleton collapse or the appearance of impurity phase (Fig. S1(b–d)†), which proves their outstanding thermal stability. The reflection peak corresponding to (200) plane does not shift to higher 2θ region, suggesting that the nanocrystalline nature along *a*-axis are well kept during the calcination.

It's worth mentioning that **FER** zeolite could not be obtained in the absence of either OTMAC or 4-DMAP (Fig. S2†), suggesting these two compounds might play a cooperative role in the crystallization of SCM-37 zeolite. ^{13}C NMR spectra of the as-synthesized SCM-37 and corresponding OTMAC and 4-DMAP are shown in Fig. 2. It can be seen that the chemical shifts at 13, 22, 25, 28, 31, 52 and 66 ppm in the ^{13}C MAS NMR spectra are assigned to $OTMA^+$, which means the SCM-37 zeolite contains a large number of $OTMA^+$, but the signals at 37, 106 and ~145 ppm belong to 4-DMAP is relatively weak. Meantime, some small signals can be seen in the ^{13}C solid-state MAS NMR spectra, the reason is not certain, it may be caused by the decomposition of a part of organic OTMAC and 4-DMAP in the synthesis process under high temperature and high pressure.

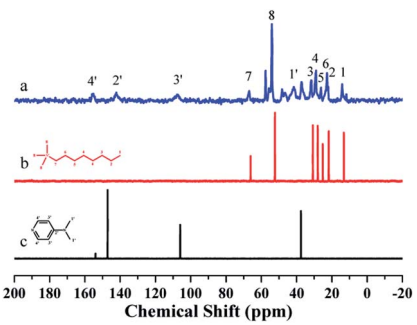

Fig. 2 ^{13}C MAS NMR patterns of the as-synthesized SCM-37 zeolite (a), OTMAC solution (b), and 4-DMAP (c).

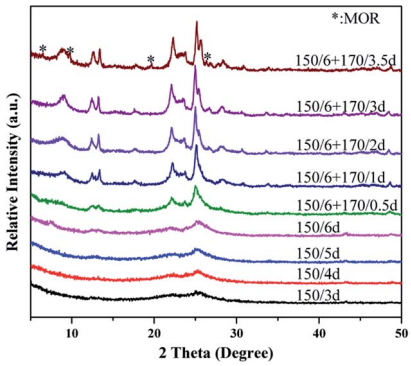

Fig. 3 XRD patterns of the as-synthesized SCM-37 zeolites crystallized for different time.

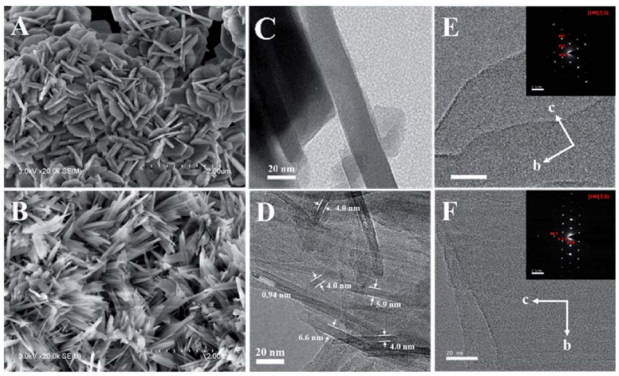

Fig. 4 SEM (A and B) and HRTEM (C–F) images of C-**FER** (A, C, E) and SCM-37 (B, D, F). The inserted images in panel E and F are the selected area electron diffraction (SAED) patterns.

The result suggests that $OTMA^+$ and 4-DMAP participate in the formation of SCM-37 zeolite as OSDA, while only a small amount of 4-DMAP entered the framework of zeolite. The 8-MR channel is possible to accommodate OTMAC, however, neither of the 8-MR or 10-MR channels can accommodate 4-DMAP. Thus, the ammonium head group of $OTMA^+$ is likely located in 8-MR, 10-MR channels and fer cages, whereas the 4-DMAP enables spacing the stacked crystals in the agglomerates.[42,43] Therefore, 4-DMAP might be located between the **FER** layers, preventing crystal growth in the *a*-direction.

The effect of crystallization temperature and time on the synthesis of SCM-37 has also been investigated. XRD patterns of samples collected after different crystallization times are shown in Fig. 3. The samples exhibit no obvious characteristic reflection peaks of **FER** zeolite when the crystallization time was less than 4 days at 150 °C, indicating the forming of amorphous phase. Weak diffraction peaks corresponding to **FER** structure appears at 5–30° when the crystallization time prolonged to 6 days. The relative crystallinity gradually improved with the increase of synthesis time.

Nevertheless, the crystallization process did not accomplish after 9 days, while prolonging the heating time to 11 days resulted in the emergence of **MOR** zeolite as impurity (Fig. S3†). This observation implied a narrow crystallization field of **FER** zeolite. We then employed a two-step crystallization procedure. The initial gel was heated at 150 °C for 6 days and then at 170 °C for various times. The intensities of diffraction peaks strengthened with the prolonged heating period and SCM-37 zeolite with high crystallinity could be obtained after crystalizing at 150 °C for 6 days followed by at 170 °C for 3 days. **MOR** zeolite emerged after the gel was heated at 170 °C for 3.5 days. If the crystallization temperature was fixed at 160 °C or 170 °C, only amorphous phases would be obtained, regardless of the crystallization time. It is speculated that the preparation of SCM-37 requires a period of crystallization at low temperature to ensure the formation of sufficient crystal nucleus. Shortening the time of crystallizaion at low temperature would result in a decrease in crystallinity probably because of reduced number of crystal nuclei generated at the initial stage. Taking advantage of the two-step crystallization method, SCM-37 zeolite with **FER** framework was successfully prepared.

The physicochemical properties of SCM-37 and C-**FER** zeolite materials were systematically studied and compared. For each SCM-37 sample, the peak at 9.4 ° is broader than that of C-**FER**, proving a shorter dimension along the [100] direction. This demonstrates that SCM-37 crystals are much thinner than C-**FER** crystals. The relative crystallinity of SCM-37 seems to be a bit lower than that of C-**FER**, due to the broadening of the diffraction peaks. The comparison of the crystal thickness of SCM-37 and C-**FER** samples can be realized by SEM and TEM techniques. As depicted in Fig. 4, C-**FER** consists of typical rectangular flake-like crystals, while SCM-37 ($SiO_2/Al_2O_3 = 25$) crystals are characterized by a nanosheet-like morphology. No amorphous phase or other zeolitic crystals could be found in the samples. TEM images (Fig. 4C) show that the thickness of C-**FER** zeolite along the *a*-axis exceeds 20 nm. In the contrary, the thickness of SCM-37 zeolite crystals is 4∼7 nm, confirming the ultrathin nature of the nanosheets. This observation is in line with the result inferred from XRD patterns. Crystals with clear lattice fringes could be observed through the HRTEM images, indicating the high crystallinity of both materials (Fig. 4E and F). In addition, sharp and clear diffraction spots in the selected area electron diffraction (SAED) indicated that the **FER** nanolayers are ordered and packed in the [100] direction.

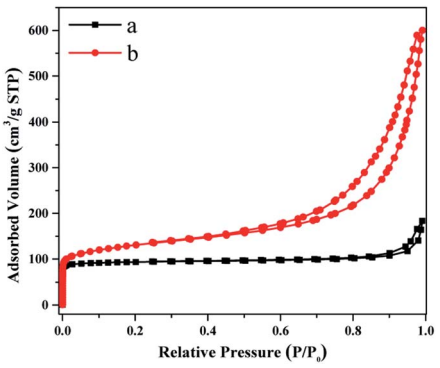

Fig. 5 N_2 adsorption–desorption isotherms of C-**FER** (a) and SCM-37 (b).

Table 1 Textural properties of C-**FER** and SCM-37 zeolites

Sample	SiO_2/Al_2O_3[a]	S_{BET}[b] ($m^2\ g^{-1}$)	S_{ext}[c] ($m^2\ g^{-1}$)	S_{micro}[d] ($m^2\ g^{-1}$)	V_{total}[e] ($cm^3\ g^{-1}$)	V_{micro}[c] ($cm^3\ g^{-1}$)
C-FER	23.9	359	18	341	0.28	0.14
SCM-37	23.1	475	198	277	0.93	0.12

[a] Measured by ICP. [b] Calculated from BET method. [c] Calculated from *t*-plot method. [d] $S_{micro} = S_{BET} - S_{ext}$. [e] Calculated from the N_2 volume adsorbed at $P/P_0 = 0.99$.

The N_2 adsorption–desorption isotherms of C-**FER** and SCM-37 ($SiO_2/Al_2O_3 = 25$) are displayed in Fig. 5, and the textural properties are summarized in Table 1. C-**FER** exhibits a type I isotherm which is characteristic of microporous materials. The total BET surface area (359 $m^2\ g^{-1}$), total pore volume (0.28 $cm^3\ g^{-1}$) and micropore volume (0.14 $cm^3\ g^{-1}$) are all close to those reported in the previous researche.[35] The external specific surface area is 18 $m^2\ g^{-1}$, which contributes little to the total specific surface area. In contrast, SCM-37 shows a type IV isotherm along with a moderate uptake of N_2 in a medium relative pressure range, as well as a remarkable capillary condensation step above a relative pressure of 0.9 due to the inter-crystal voids arising from the stacking of nanosheet crystals. The micropore volume and micropore surface area of SCM-37 are comparable, although slightly lower, to those of C-**FER**. However, the external surface area of SCM-37 reaches 198 $m^2\ g^{-1}$, which is over ten times larger than that of C-**FER**.

The NH_3-TPD curves of both **FER** zeolite materials (Fig. S4†) display two obvious desorption peaks at *ca.* 200 °C and 425 °C, corresponding to the weak and strong acid sites of the zeolites, respectively. Although the two zeolites possessed similar SAR (Table 1), the total acid amount of SCM-37 was lower than that of C-**FER** sample (955 μmol g^{-1} *vs.* 1349 μmol g^{-1}). Fig. S5† shows the Py-IR spectra of the **FER** zeolites. The calculated amounts of acid sites were listed in Table S1.† The concentrations of both B and L acid sites of C-**FER** are higher than those of SCM-37. The reason might lie in the slight lower relative crystallinity of SCM-37.[44] Furthermore, ^{27}Al MAS NMR spectra (Fig. S6†) prove that almost all Al species in both **FER** zeolites are isomorphically incorporated into the framework as deduced from the presence of the resonance at 53 ppm and the absence of octahedrally coordinated resonance around 0 ppm. After calcination, less than 5% of the Al species migrated to non-framework sites while the majority of the Al species retained within the framework, indicating excellent thermal stability of both SCM-37 and C-**FER** materials.

Fig. 6 displays the FTIR spectra of OH-stretching vibrations in the region between 3400 cm^{-1} and 3800 cm^{-1}. Both zeolites exhibit the characteristic bands at 3745 cm^{-1} ascribed to the stretching vibration of terminal silanol groups and at 3602 cm^{-1} contributed by bridging hydroxyl groups (Si–OH–Al). In addition, there is a broad peak at 3640 cm^{-1} attributed to OH groups connected to non-framework aluminum species.[45–47] The intense peak at around 3745 cm^{-1} for SCM-37 is significantly stronger than that of C-**FER**, indicating that SCM-37 is partially delaminated and an abundance of terminal silanol groups are exposed on the external surface of crystals.

The catalytic performance of SCM-37 and C-**FER** were comparatively evaluated by using the catalytic cracking of T*i*PB carried out at different temperatures. As shown in Fig. 7, the conversion of T*i*PB increased with the increasing of reaction temperature for both catalysts. The conversion of T*i*PB over C-**FER** zeolite was 27% at 250 °C and gradually rose to 50% and 94% as the reaction temperature raised to 300 °C and 350 °C. By contrast, the conversion of T*i*PB over SCM-37 was 74% at reaction temperature of 250 °C, which was pronouncedly higher than that over C-**FER**. The conversion kept climbing up to 95% at 300 °C and reached nearly 100% at 350 °C. It is widely accepted that the cracking of T*i*PB is a diffusion-controlled reaction and promoted accessibility of active sites is significant beneficial to this process. Moreover, T*i*PB molecular with a critical diameter of 0.95 nm is too bulky to diffuse into the micropore of **FER** zeolite.[48] The reaction occurs at the weak

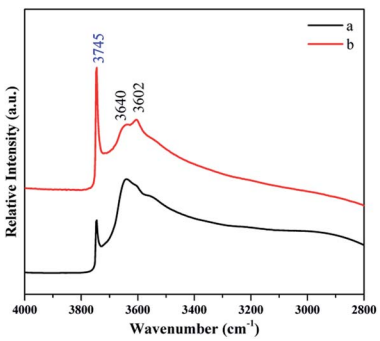

Fig. 6 FT-IR spectra of OH-stretching vibration of C-**FER** (a) and SCM-37 (b).

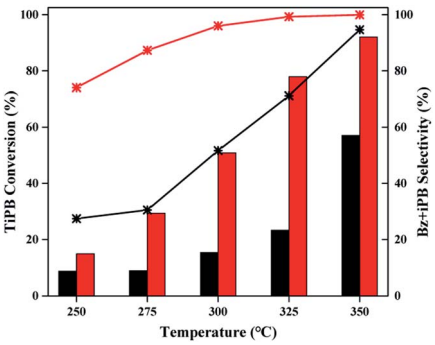

Fig. 7 Conversion of T*i*PB (asterisk line) and selectivity to Bz + *i*PB (bars) over C-**FER** (black) and SCM-37 (red) at different reaction temperatures.

Brønsted acid located on the external surface.[49–51] Taking into account the similar SiO_2/Al_2O_3 molar ratio in both **FER** zeolites and the less acid sites (especially Brønsted acid) of SCM-37 zeolite, the superior catalytic performance of SCM-37 should be related to its remarkably higher external surface area arising from the ultrathin nanosheets. The primary products in the cracking of T*i*PB are diisopropylbenzene (D*i*PB) and propylene, while the deep cracking of D*i*PB gives isopropylbenzene (*i*PB) and benzene (Bz). The selectivities to *i*PB and Bz over SCM-37 zeolite were always higher than those over C-**FER** under the same condition (Fig. 7, Table S2†). It suggests that the increased external surface area of the **FER** zeolite catalyst not only favors the cracking of T*i*PB, but also deep cracking of D*i*PB.

It is broadly believed that the high exposure of external surface of zeolite materials is beneficial to the conversion of organic molecules which are too bulky to be accommodated within the sub-nanopores of zeolites. We believe SCM-37 with ultrathin nanosheets opens up opportunity to make greater contributions to industrial catalysis processes, especially those involving heavy feeds.

Conclusions

In summary, we have developed an effective method for the direct synthesis of ultrathin **FER** zeolite nanosheets. By using OTMAC and 4-DMAP as dual templates, SCM-37 zeolite with thicknesses along the *a*-axis of 4∼7 nm was successfully prepared. The synthesis field of SCM-37 was narrow and a two-step crystallization approach offered an opportunity for the successful synthesis of pure **FER** zeolite with high crystallinity. This novel zeolite material is characterized by remarkably higher external surface area compared to conventional **FER** zeolites. Thanks to the enhanced accessibility of active sites distributed on the external surface, SCM-37 exhibited a superior performance in the catalytic cracking of T*i*PB. The new method may also offers a good avenue for the development of other zeolites with ultrathin nanosheets in the future.

Author contributions

Yuekun Li performed most experiments, analyzed all the data, and wrote the original draft. Duozheng Ma carried out part of the experiments. Wenhua Fu: data curation, formal analysis, writing – review & editing. Chuang Liu: data curation. Yu Wang: data curation. Zhendong Wang: conceptualization, methodology, funding acquisition, writing – review & editing. Weimin Yang: conceptualization, project administration, funding acquisition, resources, writing – review.

Conflicts of interest

There are no conflicts to declare.

Acknowledgements

We acknowledge the financial support from the National Key R&D Program of China (2017YFB0702800), and the National Natural Science Foundation of China (21972168, 21802168).

References

1 M. E. Davis, *Nature*, 2002, **417**, 813–821.
2 S. I. Zones, *Microporous Mesoporous Mater.*, 2011, **144**, 1–8.
3 V. Valtchev and L. Tosheva, *Chem. Rev.*, 2013, **113**, 6734–6760.
4 M. Moliner, C. Martínez and A. Corma, *Chem. Mater.*, 2014, **26**, 246–258.
5 M. Moliner, C. Martínez and A. Corma, *Chem. Mater.*, 2014, **26**, 246–258.
6 J. Shi, Y. Wang, W. Yang, Y. Tang and Z. Xie, *Chem. Soc. Rev.*, 2015, **44**, 8877–8903.
7 M. Dusselier and M. E. Davis, *Chem. Rev.*, 2018, **118**, 5265–5329.
8 A. Corma, *J. Catal.*, 2003, **216**, 298–312.
9 M. Moliner, C. Martínez and A. Corma, *Angew. Chem., Int. Ed.*, 2015, **54**, 3560–3579.
10 V. Valtchev, G. Majano, S. Mintova and J. P. Ramírez, *Chem. Soc. Rev.*, 2013, **42**, 263–290.
11 T. F. Degnan, *J. Catal.*, 2003, **216**, 32–46.
12 B. Smit and T. L. M. Maesen, *Nature*, 2008, **451**, 671–678.
13 L. Xu and J. Sun, *Adv. Energy Mater.*, 2016, **6**, 1600441.
14 S. C. Larsen, *J. Phys. Chem. C*, 2007, **111**, 18464–18474.
15 P. Chlubná, W. J. Roth, H. F. Greer, W. Zhou, O. Shvets, A. Zukal, J. Čejka and R. E. Morris, *Chem. Mater.*, 2013, **25**, 542–547.
16 J. Přech, P. Pizarro, D. P. Serrano and J. Čejka, *Chem. Soc. Rev.*, 2018, **47**, 8263–8306.
17 H. Xu, J. Zhu, L. Zhu, E. Zhou and C. Shen, *Molecules*, 2020, **25**, 3722–3739.
18 A. Korde, B. Min, E. Kapaca, O. Knio, I. Nezam, Z. Wang, J. Leisen, X. Yin, X. Zhang, D. S. Sholl, X. Zou, T. Willhammar, C. W. Jones and S. Nair, *Science*, 2022, **375**, 622–666.
19 B. Li, K. M. Kwok and H. C. Zeng, *ACS Appl. Mater. Interfaces*, 2021, **13**, 20524–20538.
20 K. Shen, X. Huang, J. Wang, Z. Chen, Y. Yu, Z. Tang and Y. Liu, *Microporous Mesoporous Mater.*, 2020, **297**, 110027.
21 H. S. Jung, N. T. Xuan and J. W. Bae, *Microporous Mesoporous Mater.*, 2021, **310**, 110669.
22 T. Xue, H. Liu and Y. Wang, *RSC Adv.*, 2015, **5**, 12131–12138.
23 H. Fjellvag, K. P. Lillerud, P. Norby and K. Sorby, *Zeolites*, 1989, **9**, 152–158.
24 R. Byggningsbacka, N. Kumar and L. E. Lindfors, *J. Catal.*, 1998, **178**, 611–620.
25 Y. Wang, Y. Gao, W. Chu, D. Zhao, F. Chen, X. Zhu, X. Li, S. Liu, S. Xie and L. Xu, *J. Mater. Chem. A*, 2019, **7**, 7573–7580.
26 Y. P. Khitev, I. I. Ivanova, Y. G. Kolyagin and O. A. Ponomareva, *Appl. Catal., A*, 2012, **441–442**, 124–135.
27 P. Wuamprakhon, C. Wattanakit, C. Warakulwit, T. Yutthalekha, W. Wannapakdee, S. Ittisanronnachai and J. Limtrakul, *Microporous Mesoporous Mater.*, 2016, **219**, 1–9.
28 M. Petersson, T. Holma, B. Andersson, E. Jobson and A. Palmqvist, *J. Catal.*, 2005, **235**, 114–127.
29 P. Cheung, A. Bhan, G. J. Sunley and E. Iglesia, *Angew. Chem., Int. Ed.*, 2006, **118**, 1647–1650.

30 J. Liu, H. Xue, X. Huang, Y. Li and W. Shen, *Catal. Lett.*, 2010, **139**, 33–37.
31 X. Li, X. Liu, S. Liu, S. Xie, X. Zhu, F. Chen and L. Xu, *RSC Adv.*, 2013, **3**, 16549–16557.
32 X. Feng, P. Zhang, Y. Fang, W. Charusiri, J. Yao, X. Gao, Q. Wei, P. Reubroycharoen, T. Vitidsant, Y. Yoneyama, G. Yang and N. Tsubaki, *Catal. Today*, 2020, **343**, 206–214.
33 A. B. Pinar, P. A. Wright, L. Gómez-Hortigüela and J. Pérez-Pariente, *Microporous Mesoporous Mater.*, 2010, **129**, 164–172.
34 S. J. Xie, J. B. Peng, L. Y. Xu, Z. H. Wu and Q. X. Wang, *Chin. J. Catal.*, 2003, **24**, 531–534.
35 W. Chu, F. Chen, C. Guo, X. Li, X. Zhu, Y. Gao, S. Xie, S. Liu, N. Jiang and L. Xu, *Chin. J. Catal.*, 2017, **38**, 1880–1887.
36 X. X. Chen, T. Todorova, A. Vimont, V. Ruaux, Z. X. Qin, J. P. Gilson and V. Valtchev, *Microporous Mesoporous Mater.*, 2014, **200**, 334–342.
37 Y. Lee, M. B. Park, P. S. Kim, A. Vicente, C. Fernandez, I.-S. Nam and S. B. Hong, *ACS Catal.*, 2013, **3**, 617–621.
38 V. J. Margarit, M. R. D. Rey, M. T. Navarro, C. Martínez and A. Corma, *Angew. Chem., Int. Ed.*, 2018, **57**, 3459–3464.
39 T. Xue, S. Li and H. Wu, *Microporous Mesoporous Mater.*, 2020, **312**, 110748.
40 H. Xu, W. Chen, G. Zhang, P. Wei, Q. Wu, L. Zhu, X. Meng, X. Li, J. Fei, S. Han, Q. Zhu, A. Zheng, Y. Ma and F. Xiao, *J. Mater. Chem. A*, 2019, **7**, 16671–16676.
41 M. Peng, Z. Wang, J. Huang, M. Shen, J. Jiang, H. Xu, Y. Ma, B. Hu, X. Gong, H. Wu and P. Wu, *Chem. Mater.*, 2021, **33**, 6934–6941.
42 R. García, L. Gómez-Hortigüela, I. Díaz, E. Sastre and J. Pérez-Pariente, *Chem. Mater.*, 2008, **20**, 1099–1107.
43 R. García, L. Gómez-Hortigüela, T. Blasco and J. Pérez-Pariente, *Microporous Mesoporous Mater.*, 2010, **132**, 375–383.
44 K. Kim, R. Ryoo, H.-D. Jang and M. Choi, *J. Catal.*, 2012, **288**, 115–123.
45 A. Bolshakov, R. Poll, T. Bergen-Brenkman, S. Wiedemann, N. Kosinov and E. Hensen, *Appl. Catal., B*, 2020, **263**, 118356.
46 P. Wu, J. Ruan, L. Wang, L. Wu, Y. Wang, Y. Liu, W. Fan, M. He, O. Terasaki and T. Tatsumi, *J. Am. Chem. Soc.*, 2008, **130**, 8178–8187.
47 A. Bonilla, D. Baudouin and J. Pérez-Ramírez, *J. Catal.*, 2009, **265**, 170–180.
48 S. Mi, T. Wei, J. Sun, P. Liu, X. Li, Q. Zheng, K. Gong, X. Liu, X. Gao, B. Wang, H. Zhao, H. Liu and B. Shen, *J. Catal.*, 2017, **347**, 116–126.
49 M. S. Aghakhani, A. A. Khodadadi, Sh. Najafi and Y. Mortazavi, *J. Ind. Eng. Chem.*, 2014, **20**, 3037–3045.
50 S. Zhao, D. Collins, L. Wang and J. Huang, *Catal. Today*, 2021, **368**, 211–216.
51 Q. Wang, L. Zhang, Z. Yao, Y. Guo, Z. Gao, J. Zheng, W. Li, B. Fan, Y. Wang, S. Chen and R. Li, *Mater. Chem. Phys.*, 2020, **243**, 122610.